



HAL
open science

Radiation dose reduction with dictionary learning based processing for head CT.

Yang Chen, Luyao Shi, Jiang Yang, Yining Hu, Limin Luo, Xindao Yin,
Jean-Louis Coatrieux

► **To cite this version:**

Yang Chen, Luyao Shi, Jiang Yang, Yining Hu, Limin Luo, et al.. Radiation dose reduction with dictionary learning based processing for head CT.. Australasian Physical and Engineering Sciences in Medicine, 2014, 37 ((3)), pp.483-93. 10.1007/s13246-014-0276-7 . inserm-01007561

HAL Id: inserm-01007561

<https://inserm.hal.science/inserm-01007561>

Submitted on 16 Jun 2014

HAL is a multi-disciplinary open access archive for the deposit and dissemination of scientific research documents, whether they are published or not. The documents may come from teaching and research institutions in France or abroad, or from public or private research centers.

L'archive ouverte pluridisciplinaire **HAL**, est destinée au dépôt et à la diffusion de documents scientifiques de niveau recherche, publiés ou non, émanant des établissements d'enseignement et de recherche français ou étrangers, des laboratoires publics ou privés.

Radiation Dose Reduction With Dictionary Learning Based Processing for Head CT

Yang Chen^{1,2,3}, Luyao Shi^{1,2,3}, Jiang Yang⁴, Yining Hu^{1,2,3}, Limin Luo^{1,2,3}, Xindao Yin⁵, Jean-Louis Coatrieux^{3,6,7},

1. Laboratory of Image Science and Technology, Southeast University, 210096, Nanjing, People's Republic of China
2. The Key Laboratory of Computer Network and Information Integration (Southeast University), Ministry of Education.
3. Centre de Recherche en Information Biomedicale Sino-Francais (LIA CRIBs), Rennes, France
4. Key Laboratory of Photoelectronic Imaging Technology and System, Ministry of Education
5. Department of Radiology, Nanjing Hospital Affiliated to Nanjing Medical University, 210096, People's Republic of China.
6. INSERM, U1099, Rennes, F-35000, France;
7. Université de Rennes 1, LTSI, Rennes, F-35000, France.

BACKGROUND AND PURPOSE: In CT, ionizing radiation exposure from the scan has attracted much concern from patients and doctors. This work is aimed at improving head CT images from low-dose scans by using a fast DL based post-processing.

MATERIALS AND METHODS: Both LDCT and SDCT nonenhanced head images were acquired in head examination from a multi-detector row Siemens Somatom Sensation 16 CT scanner. 100 patients were involved in the experiments. Two groups of LDCT images were acquired with 50% (LDCT50%) and 25% (LDCT25%) tube current setting in SDCT. To give quantitative evaluation, SNR and CNR were computed from the HU measurements of GM, WM and CSF tissues. A blinded qualitative analysis was also performed to assess the processed LDCT datasets.

RESULTS: 50% and 75% dose reductions are obtained for the two LDCT groups (LDCT50%, 1.15 ± 0.1 mSv; LDCT25%, 0.58 ± 0.1 mSv; SDCT, 2.32 ± 0.1 mSv; $P < 0.001$). Significant SNR increase over the original LDCT images is observed in the processed LDCT images for all the GM, WM and CSF tissues. Significant GM-WM CNR enhancement is noted in the DL processed LDCT images. Higher SNR and CNR than the reference SDCT images can even be achieved in the processed LDCT50% and LDCT25% images. Blinded qualitative review validates the perceptual improvements brought by the proposed approach.

CONCLUSIONS: Compared to the original LDCT images, the application of DL processing in head CT is associated with a significant improvement of image quality.

ABBREVIATIONS:

LDCT = low-dose CT; SDCT = standard-dose CT; DL = dictionary learning; K-SVD = k-means singular value decomposition; SD = standard deviation; SNR = signal to noise ratio; CNR = contrast to noise ratio; $CTDI_{vol}$ = volume CT dose index; DLP = dose length product; ED = effective dose; FBP = filtered back-projection; mA = milliamperere; mAs = milliamperere second; HU = Hounsfield unit; ASIR = adaptive statistical iterative reconstruction; PICCS = prior image constrained compressed sensing; ROI = region of interest.

1. Introduction

The radiation doses delivered to patients during X-ray CT examinations are relatively high when compared to other radiological examinations [1-3]. Over recent years, due to the ever-increasing CT utilization in clinical diagnosis, there has been increasing concern about the long term effects of exposure to ionizing radiation. The dose in CT is cumulative over a lifetime, and successive CT scanning can significantly increase the lifetime radiation risk of fatal cancers [4].

LDCT is therefore of major importance in order to alleviate the harm caused by cumulated radiation exposure for the patients. Low-dose CT protocols should attempt to balance image quality with radiation dose savings. Among all the methods proposed so far to obtain LDCT images, the most practical and widely used method is lowering the X-ray tube current by modulating the setting of mA or mAs. However, an arbitrary reduction in ionizing radiation may result in

significant deterioration of image quality and may render CT studies clinically unacceptable [5-6].

In the past ten years, some iterative reconstruction (IR) algorithms were introduced to CT to reduce image noise and artifacts, therefore allowing significant dose reduction [7-18]. IR approaches solve the problem via maximizing a prior-regularized cost function using iterative optimizations [7-12]. Clinical potential of IR algorithms has been well demonstrated by the prior image constrained compressed sensing (PICCS) algorithm [12], the adaptive statistical iterative reconstruction (ASIR) algorithm [13-16] and the iDose algorithm [17]. For head CT, around 20%-45% dose reduction without compromising diagnostic accuracy was reported for IR algorithms in several studies [14-17], which is rather modest when compared to abdominal and thoracic applications (50%-75%) [18-19].

However, the most well-known drawback for IR is the intensive computation cost often required for reconstruction, which is about 10-50 times larger than that of the widely-used analytic FBP algorithm. Also, due to the difficult access to well-formatted projection data of most CT vendors, research on reconstruction approaches is often highly limited in practice. Additionally, the CT scanners equipped in most current hospitals are based on FBP algorithms and upgrading to the latest CT scanners with IR algorithms is often not affordable for most small or medium-sized hospitals.

Compared to IR type solutions to LDCT imaging, post-processing methods require much less computation cost and always have easy implementation to most current CT systems. The objective of post-processing based LDCT application is to obtain images with visual appearances close to the corresponding SDCT images without blurring important structures and introducing new artifacts. However, due to the fact that the back-projection process in the FBP algorithm distributes the noise and artifacts non-uniformly over the whole image, CT noise and artifacts with mottled or streak effects are often difficult to be removed from already reconstructed images.

In recent years, there has been growing interest in the study of sparse and redundant representations over dictionary learning [20-27]. Some successful applications in medical imaging have been explored [28-35]. They concerned undersampled MRI image reconstruction [28], resolution enhancement [29], interior tomography [30], DL constrained iterative LDCT reconstruction [31], 3-D medical image denoising [32], few-views tomography [33], spectral CT [34] and abdomen LDCT image processing [35]. The patch-wise based processing in DL approach inherently enables an effective representation of patch-shaped features such as parenchyma and tumor tissues. In the paper, we propose to improve head LDCT images through applying such DL processing. The proposed DL algorithm can be efficiently implemented by using a global dictionary. In the validation, clinical LDCT images from a large set of patients were used, and the corresponding SDCT images were acquired as well to provide a ground truth reference.

2. Material and Methods

Patient Sample, Scan Protocol and Dose Parameters

The protocol of this study (data collection and post-processing) was approved by our institutional ethical review board. 50 patients were involved in the experiments. All these patients have given their written consent to the participation. A non-conflict of interest for this work was declared. CT images were acquired on a multi-detector row Siemens Somatom Sensation 16 CT scanner. The dose parameters are given in Table.1.

The 50 patients were divided into two groups. The first group (tagged as **LDCT50%**) includes 13 men and 12 women with an average age of 67 years (age range: 52-77 years), and the LDCT images were collected using a reduced tube current 80mAs under head scan protocol. For the second group (tagged as **LDCT25%**), LDCT images were collected using a reduced tube current 40mAs under head scan protocol, and this group includes 9 men and 16 women with an average age of 64 years (age range: 56-78 years). For all 50 patients covering both groups, the head scans were repeated using 160 mAs for the SDCT head scan protocol. The gantry angle in scans is with “Hard Palate” mode based on the definition in [36].

Other scan parameters include: kVp, 120; slice thickness, 6mm; Gantry rotation time, 0.5s; detector configuration (detector rows×section thickness), 16mm×1.5mm; pixel spacing: 0.4922mm×0.4922mm; table feed per gantry rotation, 24mm; pitch, 1:1; reconstruction method: FBP algorithm with convolution kernel “H31s” (“H31s” is the routine smoothing kernel used in reconstructing head images on Siemens CT). The averaged slice number for each patient scan is 40. All the CT images were exported as DICOM files and then processed offline under a PC workstation (Intel Core™ 2 Quad CPU and 4096 Mb RAM) with MATLAB (MATLAB 2012, Mathworks) as the developing language. We also accelerate the loop calculations in the DL processing using MATLAB Parallel Computing Toolbox™, which exploits the full computation potential of multicore CPU processors. About 1 second is required to process one slice. We recorded the accumulated doses from the workstation for each scan. The CTDI_{vol} and DLP were recorded for every CT examination. Effective dose (milli Sievert, mSv) was estimated by multiplying the dose-length product (DLP) with a constant region-specific conversion coefficient of 0.0021mSv/(mGy×cm) [37-38]. All the dose information is illustrated in Table 1.

	SDCT	LDCT50%	LDCT25%	P
Tube current (mAs)	160	80	40	----
Age	68 ± 16	67 ± 12	69 ± 15	0.61
Sex (male/female)	22 / 28	13 / 12	9 / 16	< 0.001
CTDI _{vol} (mGy)	61.44 ± 1.48	31.04 ± 0.93	15.38 ± 0.86	----
DLP(mGy.cm)	1196.75 ± 64.85	596.26 ± 42.72	250.36 ± 37.44	< 0.001
Effective dose (mSv)	2.51 ± 0.14	1.25 ± 0.00	0.53 ± 0.08	< 0.001

Table 1. Dose parameters

Theory and Method

Sparse representation and dictionary learning are closely related to each other in the framework of compress sensing theory. Compared to other restoration methods based on pixel-wise intensity update, patch-wise DL processing enables a more effective representation of patch-shaped features such as tumors or organs. The DL processing assumes the overlapping patches in the target LDCT images are sparsely representable, and is carried out by coding each patch as a linear combination of only a few atoms from a trained dictionary [35]. The DL method first finds the best global over-complete dictionary and then represents each image patch as a linear combination of only a few dictionary vectors (atoms). The proposed DL processing was performed on 2-D slices because the Z-axis structure continuity cannot be well preserved with the large slice thickness setting in routine head CT scanning (6mm in this work). Often with smaller sparse coefficients compared to normal image features, noise and artifacts can be suppressed in this DL process. Based on [25] and [35], the patch-based DL processing aims at solving the following problem:

$$\min_{x,D,\alpha} \|x - y\|_2^2 + \mu \sum_j \|R_j x - D\alpha_j\|_2^2 \quad \text{s.t.} \quad \|\alpha_j\|_0 \leq T \quad \forall i, j \quad (1)$$

where, x and y denote the processed and the original LDCT images respectively, and the subscript ij denotes the pixel index (i, j) in the image. R_j represents the operator that extracts the patch x_{ij} of size $n \times n$ (centered at (i, j)) from image x . The patch-based dictionary D is an $m \times K$ matrix with $m = n \times n$, which is composed of K m -vector atoms (columns). Each n -vector column corresponds to one $n \times n$ patch. α denotes the coefficient set $\{\alpha_{ij}\}_{ij}$ for all the sparse representations of patches, and each patch x_{ij} can be approximated by a linear combination. In (1), $\|\cdot\|_2^2$ is the l^2 norm and $\|\cdot\|_0$ denotes the l^0 norm that counts the nonzero entries of vector α_{ij} . T is the preset parameter of sparsity level that limits the maximum nonzero entry number in α_{ij} . Based on [23], solving (1) includes steps (2) and (3):

$$\min_{D,\alpha} \mu \sum_j \|R_j x - D\alpha_j\|_2^2 \quad \text{s.t.} \quad \|\alpha_j\|_0 \leq T \quad \forall i, j \quad (2)$$

$$\min_x \|x - y\|_2^2 + \mu \sum_j \|R_j x - D\alpha_j\|_2^2 \quad (3)$$

Here, equation (2) is solved by the K-means Singular Value Decomposition (K-SVD) method to estimate the coefficients α and dictionary D [24]. Then, we can solve the output image x by setting the first order derivative of (3) to zero (with respect to x):

$$x = \left(I + \mu \sum_j R_j^T R_j \right)^{-1} \left(y + \mu \sum_j R_j^T D \alpha_j \right) \quad (4)$$

It was pointed out in [24] that the dictionary trained from the original noisy image itself can lead to better noise suppression than using a global dictionary trained from the other available images in the database. However, in [35], we also found that the dictionary trained from a typical SDCT abdomen image always leads to visually close LDCT images when compared to the dictionary trained from the LDCT image itself. The reason might be that most CT images are often composed of similar human tissues in rather low numbers, and that the dictionary discrepancy caused by the differences between different CT images only leads to tiny differences in the sparsified features. For one specific LDCT head image, organs or other human tissues can be efficiently represented by the dictionary atoms learned from some other head CT images. Thus, in this study we use a pre-calculated dictionary D_p (the left image in Fig.1) trained from one typical SDCT head image (the right image in Fig.1). Each element in D_p is of certain size and defined as atom [24]. One important merit of this approach is that the intensive computation required in dictionary training can be avoided with this pre-calculated global dictionary. Here, 8×8 overlapping patches ($3.94\text{mm} \times 3.94\text{mm}$, $n = 8$) are set to allow an effective representation of local organ or lesion tissues, and the atom number K is set to 64 for it is found large enough to represent the tissue

structures in head CT images. The whole DL processing can be defined by the following two steps:

$$(S1), \quad \min_{\alpha} \sum_j \|\alpha_j\|_0 \quad \text{s.t.} \quad \|R_j x - D_p \alpha_j\|_2^2 \leq \varepsilon \quad \forall i, j \quad (5)$$

$$(S2), \quad \min_x \|x - y\|_2^2 + \mu \sum_j \|R_j x - D_p \alpha_j\|_2^2 \quad (6)$$

Here, with the pre-trained dictionaries D_p , the solution defined in (2) and (3) is transformed to (5) and (6), in which the sparse coefficient set α and the image x can be calculated using the orthogonal matching pursuit (OMP) algorithm and the solution given in (4). In (5), ε denotes the tolerance parameter used in calculating α by OMP method. The parameters involved in the proposed DL methods were specified under the guidance of one radiological doctor (Y.D. with 15 years of experience) to provide the best visual results. Practically, we found that the same parameter setting can be used to process the LDCT images with the same scan protocol, and this is due to the similar distribution of noise and artifacts for the same scanning protocol. With the global dictionary pre-trained, around 1 second is required to process one single 2-D slice.

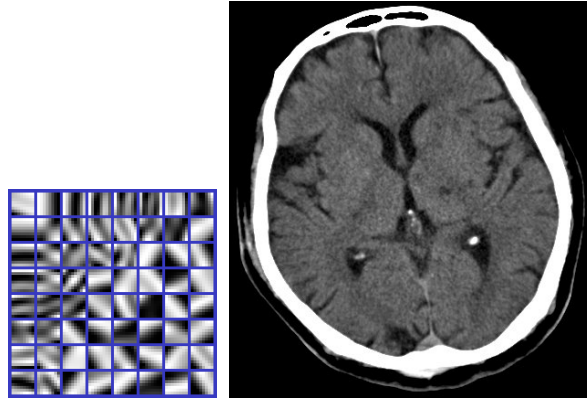


Fig.1 The left picture is the trained dictionary used in this study with $m = n \times n = 8 \times 8 = 64$ ($n = 8$) and $K = 64$. The right image corresponds to the SDCT head image from which the global dictionary was trained.

Quantitative Image Analysis

Two metrics, SNR and CNR, were calculated to give quantitative analysis of the image quality. SNR is regarding the GM, WM and CSF tissues, and CNR quantifies the differentiation property between GM and WM tissues in head CT images. 10 images in total were selected from the dataset for this quantitative calculation. As illustrated in Fig.2, one pair of ROI of mean area 44mm^2 (ROI-1 and ROI-2) were placed in lentiform nucleus and the adjacent corpus callosum for GM and WM tissues, respectively; another pair of ROIs of mean area 32mm^2 (ROI-3 and ROI-4) were placed in dorsal thalamus and the adjacent optic radiation fiber tissue for GM and WM tissues, respectively. The GM and WM ROI (ROI-1, ROI-2, ROI-3 and ROI-4) were selected from the images of a subgroup of patients (15 patients in LDCT50% group and 16 patients in LDCT25% group) that allows suitable ROI drawing. Also, the CSF ROIs (ROI-5, mean area 15mm^2) were selected in a subgroup (19 patients in LDCT50% group and 17 patients in LDCT25% group) of patients whose lateral ventricles are suitable for ROI drawing. We use the GM-WM CNR1 to represent the CNR between ROI-1 and ROI-2, and use the GM-WM CNR2 to represent the CNR between ROI-3 and ROI-4. With HU as the unit value, the SD, SNR and GM-WM CNR were calculated using the following equations:

$$SD_{\Omega} = \sqrt{\frac{1}{|\Omega| - 1} \sum_{ij \in \Omega} (x_{ij} - \bar{x}_{\Omega})^2} \quad (7)$$

$$SNR = \frac{\bar{x}_{\Omega}}{SD_{\Omega}} \quad (8)$$

$$GM-WM \text{ CNR} = \frac{\bar{x}_{\Omega}^{GM} - \bar{x}_{\Omega}^{WM}}{\sqrt{(SD_{\Omega}^{GM})^2 + (SD_{\Omega}^{WM})^2}} \quad (9)$$

where, x_{ij} and \bar{x}_{Ω} denote each HU value and the averaged HU value within ROI defined by Ω , respectively. $|\Omega|$ is the

pixel number in Ω . $\bar{x}_{\Omega}^{\text{GM}}$ and $\bar{x}_{\Omega}^{\text{WM}}$ denote the averaged HU within the ROIs for GM and WM tissues, respectively. $\text{SD}_{\Omega}^{\text{GM}}$ and $\text{SD}_{\Omega}^{\text{WM}}$ denote the SD within the ROI for GM and WM tissues, respectively.

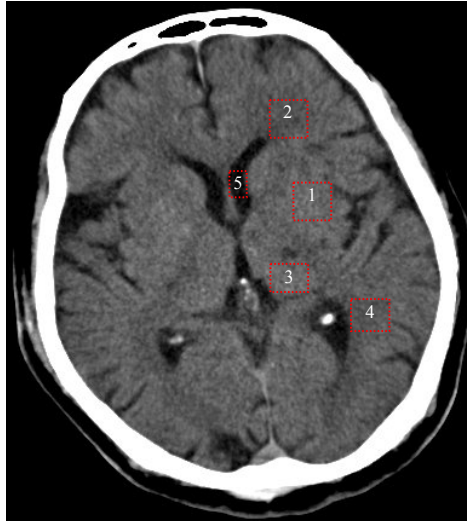


Fig.2. Illustration of ROI-1, ROI-2, ROI-3, ROI-4 and ROI-5 for quantitative analysis in an axial CT plane.

Qualitative Image Analysis

For qualitative assessment, 100 original images (including 50 LDCT and 50 SDCT images), 100 processed images (including 50 processed LDCT50% and 50 processed LDCT25% images) are considered. A window with level 40HU and width 80HU is used here. 5 subjective features, noise suppression, artifact suppression, contrast preservation, tissue discrimination and overall image quality, were evaluated using a five-point subjective scale (1=unacceptable, 2=substandard, 3=acceptable, 4=above average, 5=excellent). Here, we define artifacts as any structures having a passive effect on subjective diagnosis. Three radiological readers (Y.H. with 10 years of experience, D.M. with 8 years of experience, Y.D. with 15 years of experience.) independently evaluated the randomized set of LDCT images, SDCT images, and the DL processed LDCT images in a digital DICOM archiving workstation (ViewDEX 2.0 [39]). So, the five subjective features were assessed for all the 200 images (100 original and 100 processed CT images). This results in 3000 parameter ratings in total (5 image quality parameters together and the 3 readers, i.e. $200 \times 5 \times 3 = 3000$). For each subset of images, the 5 image scores were reported as means \pm SDs (averaged scores of the 3 radiologists \pm standard deviations). The subjective quality parameters of the original LDCT images and the processed LDCT images were compared with those of the reference SDCT images, in which the discrepancy between the two groups was evaluated by the Student t test with $P < 0.05$ considered as a statistically significant difference.

3. Results

Visual assessment

Fig.3 provides the processed head LDCT50% results of three patients. The first, second and third columns correspond to the original LDCT50% images (A1, A2, A3), the original SDCT images (B1, B2, B3) and the DL processed LDCT50% images (C1, C2, C3). To be specific, the first and second rows in Fig.3 depict images with ganglia lacunar infarction (see red arrows); the third row illustrates images with cerebral hemorrhage (see red arrows). Also, Fig.4 provides the processed LDCT25% results of another three patients. The first, second and third columns correspond to the original LDCT25% images (A1, A2, A3), the original SDCT images (B1, B2, B3) and the DL processed LDCT25% images (C1, C2, C3). In Fig.4, all the three rows depict images with lacunar infarction (see upper red arrows). To be specific, the lacunar infarction is in the right corona radiata in the top row; the lacunar infarction is in the lateral aspect of the left thalamus in the middle and the third rows. In addition, the two lower arrows also point to intraventricular hemorrhage in the third row.

We can clearly see that a significant improvement of image quality is obtained by the proposed DL algorithm. In the processed LDCT images, both noise and artifacts are observed to be effectively suppressed, which leads to better conspicuity of brain tissues and pathological changes (see the basal ganglia lacunar infarction and cerebral hemorrhage pointed by red arrows in Fig.3-4). Compared to the original LDCT images, the processed LDCT images present textures

visually close to the SDCT images. There was no significant difference between SDCT and LDCT50% in the detection of anatomical structures, infarction and hemorrhage changes in the brain. Nevertheless, we can also observe some tissue blurring and residual artifact traces in the processed LDCT25% images (indicated by yellow arrows in C1, C2 and C3 in Fig.4).

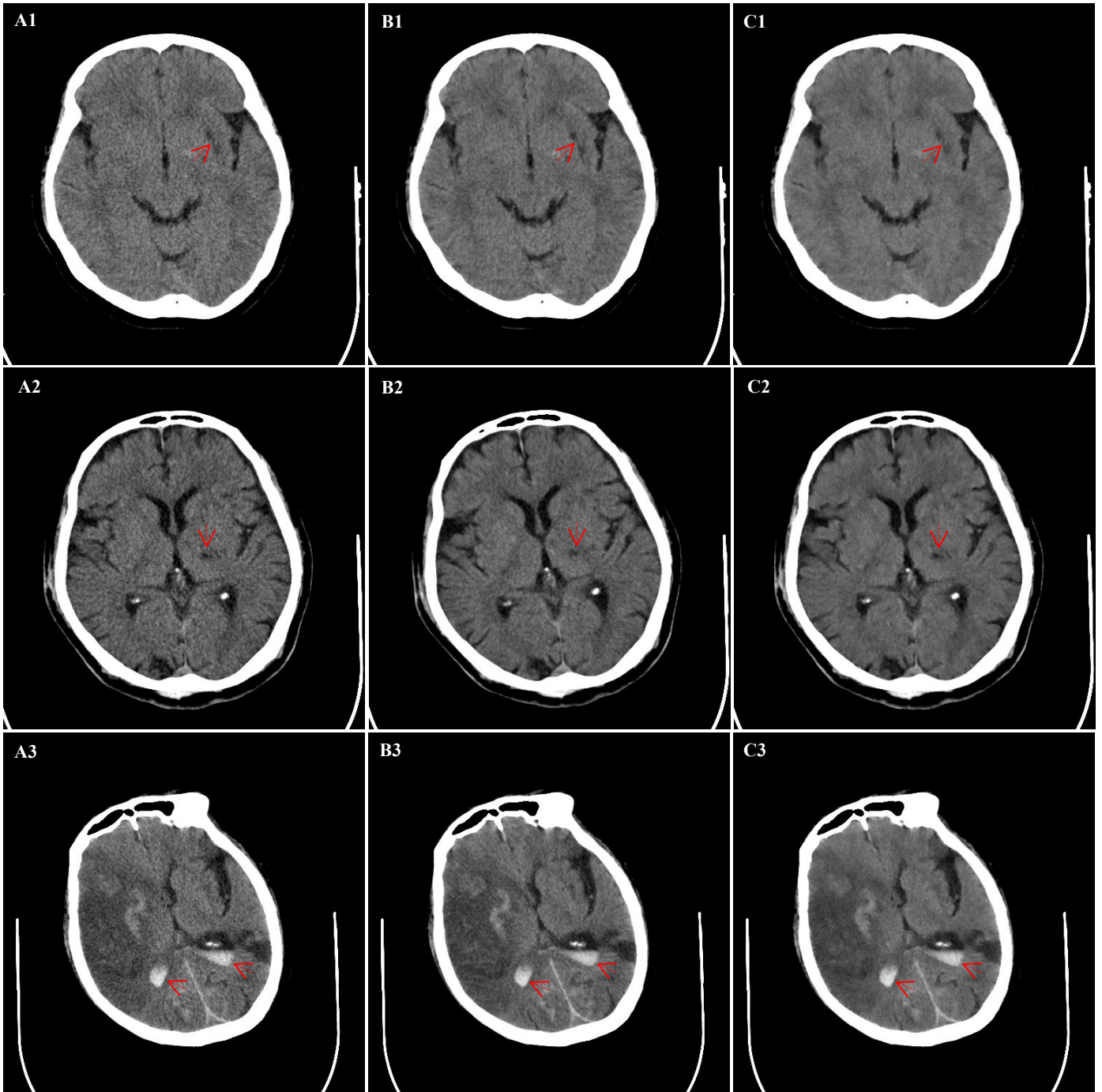


Fig.3 Processing results of head CT images for three patients (in the three rows). The first, second and third columns correspond to the original LDCT50% images (80mAs, A1, A2, A3), the original SDCT images (160mAs, B1, B2, B3), and the DL processed LDCT50% images (C1, C2, C3). The first and the second rows illustrate the CT images with basal ganglia lacunar infarction (see red arrows); the third row illustrates the CT images with cerebral hemorrhage (see the red arrows).

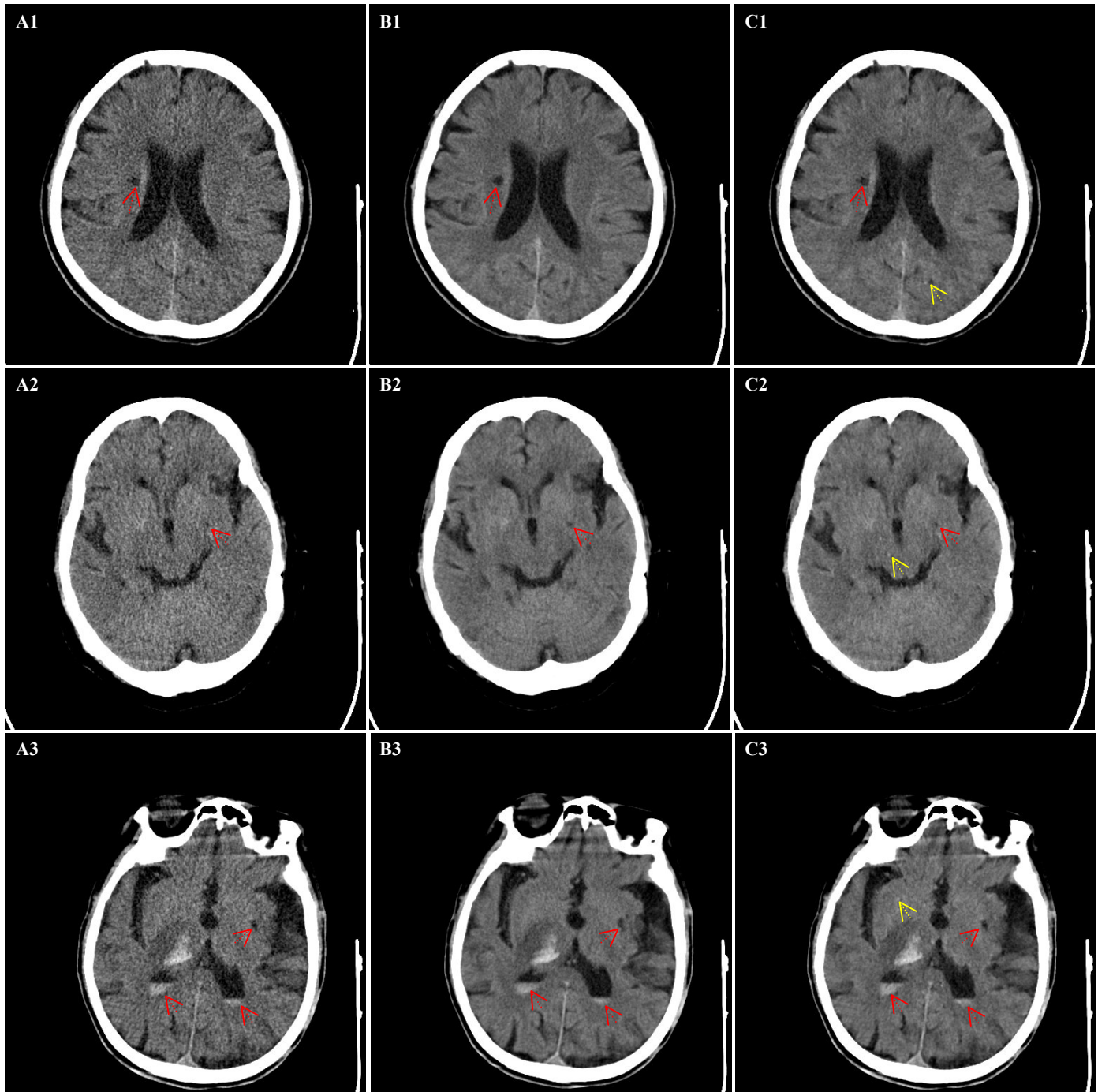


Fig.4 Processing results of head CT images for three patients (in the three rows). The first, second and third columns correspond to the original LDCT25% images (40mAs, A1, A2, A3), the original SDCT images (160mAs, B1, B2, B3), and the DL processed LDCT images (C1, C2, C3). All the first, second and the third rows illustrate the CT images with basal ganglia lacunar infarction (see red arrows); the third row also illustrates the CT images with basal ganglia infarction (see the lower two red arrows in C3). Note the yellow arrows in (C1, C2, C3) point to some residual high-contrast artifacts which are hard to be suppressed.

Quantitative assessment

The mean GM, WM and CSF attenuation values for the LDCT50% group, LDCT25% group, and SDCT group are illustrated in Table 2. Quantitative evaluation results are listed in Table.3 as the mean values \pm SD of all the patient cases. For the GM, WM and CSF tissues, we can see tube current reduction leads to significant decrease of the SNR and GM-WM CNR from the SDCT group to the LDCT50% and LDCT25% groups ($P < 0.05$). Otherwise, a significant increase of the mean SNR and GM-WM CNR is observed in the processed LDCT images with respect to the original LDCT images ($P < 0.05$).

We can see in Table.3 that the DL processing can compensate the degradation for the LDCT25% images, which shows no significant difference in SNR and CNR values from the SDCT images ($P=0.16$). Table.3 also shows the DL processing leads to significantly higher SNR and CNR for the processed LDCT50% images than the SDCT images ($P<0.05$).

	LDCT25%	LDCT50%	SDCT	Processed LDCT50%	Processed LDCT25%
GM mean (HU)	33.77 ± 0.88	33.42 ± 1.15	33.38 ± 0.93	33.19 ± 0.99	33.47 ± 0.94
WM mean (HU)	27.72 ± 1.32	27.30 ± 1.08	27.00 ± 1.16	27.43 ± 1.03	27.43 ± 1.40
CSF mean (HU)	5.14 ± 0.17	5.55 ± 0.33	5.50 ± 0.03	5.62 ± 0.23	5.66 ± 0.41

Table 2. Mean attenuation values in ROI

	LDCT25%	LDCT50%	SDCT	Processed LDCT50%	Processed LDCT25%
GM SNR	5.99 ± 0.42 *	7.97 ± 0.79 *	10.92 ± 1.29	15.81 ± 2.04 *	11.64 ± 0.74
WM SNR	5.28 ± 0.52 *	7.38 ± 0.24 *	9.99 ± 0.54	13.47 ± 1.39 *	10.07 ± 0.72
CSF SNR	1.10 ± 0.29 *	1.63 ± 0.57 *	2.12 ± 0.43	3.04 ± 0.92 *	2.21 ± 0.67
GM-WM CNR₁	0.96 ± 0.04 *	1.34 ± 0.01 *	1.81 ± 0.19	2.67 ± 0.14 *	1.89 ± 0.23
GM-WM CNR₂	0.68 ± 0.13 *	0.96 ± 0.27 *	1.34 ± 0.13	1.94 ± 0.35 *	1.41 ± 0.06

* means significantly different from the mean scores for the reference SDCT images ($P<0.05$).

Table 3. Quantitative analysis result

Qualitative assessment

The qualitative scoring result is given in Table.4. All the three observers pointed out that the reduced tube currents lead to severe degradation of CT images, and the original LDCT images are of lower quality than the original SDCT images. For all the 5 scores, statistically significant differences with respect to the reference SDCT images are noticed in all the subjective scores for both the LDCT50% and LDCT25% images ($P<0.05$). The LDCT50% images obtain higher mean scores than the LDCT25% images. We can also see in Table 4 that the processed LDCT images have quality scores substantially higher than the original LDCT images. The differences between the processed LDCT50% images with reference to the original SDCT images are found not to be statistically significant ($P=0.18$) for all the subjective scores. As to the processed LDCT25% images, significant differences with the original SDCT images are still noted for the scores of contrast preservation and tissue discrimination ($P<0.05$), and other scores are found not to be significantly different ($P=0.12$). To evaluate the overall concordance/agreement between the 3 readers on above subjective evaluations, we perform K test, and find there is substantial agreement among all the readers (Table.5, $K>0.6$, two-sided $P<0.05$).

	LDCT25%	LDCT50%	SDCT	Processed LDCT50%	Processed LDCT25%
Noise Suppression	1.92 ± 0.31 *	2.35 ± 0.26 *	3.94 ± 0.22	3.99 ± 0.16	3.78 ± 0.25
Artifact Suppression	2.07 ± 0.28 *	2.41 ± 0.24 *	3.89 ± 0.19	4.02 ± 0.23	3.65 ± 0.29
Contrast Preservation	1.75 ± 0.30 *	2.46 ± 0.37 *	3.81 ± 0.24	3.78 ± 0.24	3.53 ± 0.27 *
Tissue Discrimination	1.66 ± 0.33 *	2.36 ± 0.31 *	3.86 ± 0.27	3.75 ± 0.28	3.51 ± 0.33 *
Overall Image Quality	1.72 ± 0.28 *	2.32 ± 0.36 *	3.95 ± 0.25	3.90 ± 0.29	3.68 ± 0.32

* means significantly different from the mean scores for the reference SDCT images ($P<0.05$).

Table 4. Image Quality Scores (mean ± SDs)

K test	Noise Suppression	Artifact Suppression	Contrast Preservation	Tissue Discrimination	Overall Image Quality
K	0.631	0.672	0.659	0.638	0.652

Table 5. Averaged statistically agreement between the assessments of the 3 readers

Sensitivity analysis for dictionary training

In this section, we analyze the sensitivity of the proposed DL approach to different dictionary options. The LDCT images in Fig.3 (the first two columns) are illustrated in the same HU windows as the illustrations in above Fig.3 and Fig.4. A1, A2 and A3 in Fig.5 illustrate the DL processed images using the dictionaries trained from the LDCT images themselves. B1, B2 and B3 in Fig.5 illustrate the DL processed images using the above global dictionary. The same parameters are used in these two groups of experiment here. C1, C2 and C3 display the difference images between A1, A2, and A3 and B1, B2 and B3 in Fig.5. We can see in Fig.5 that a global dictionary can lead to almost the same result as the dictionary trained from the LDCT image itself, which validates the application of the proposed global dictionary in this study.

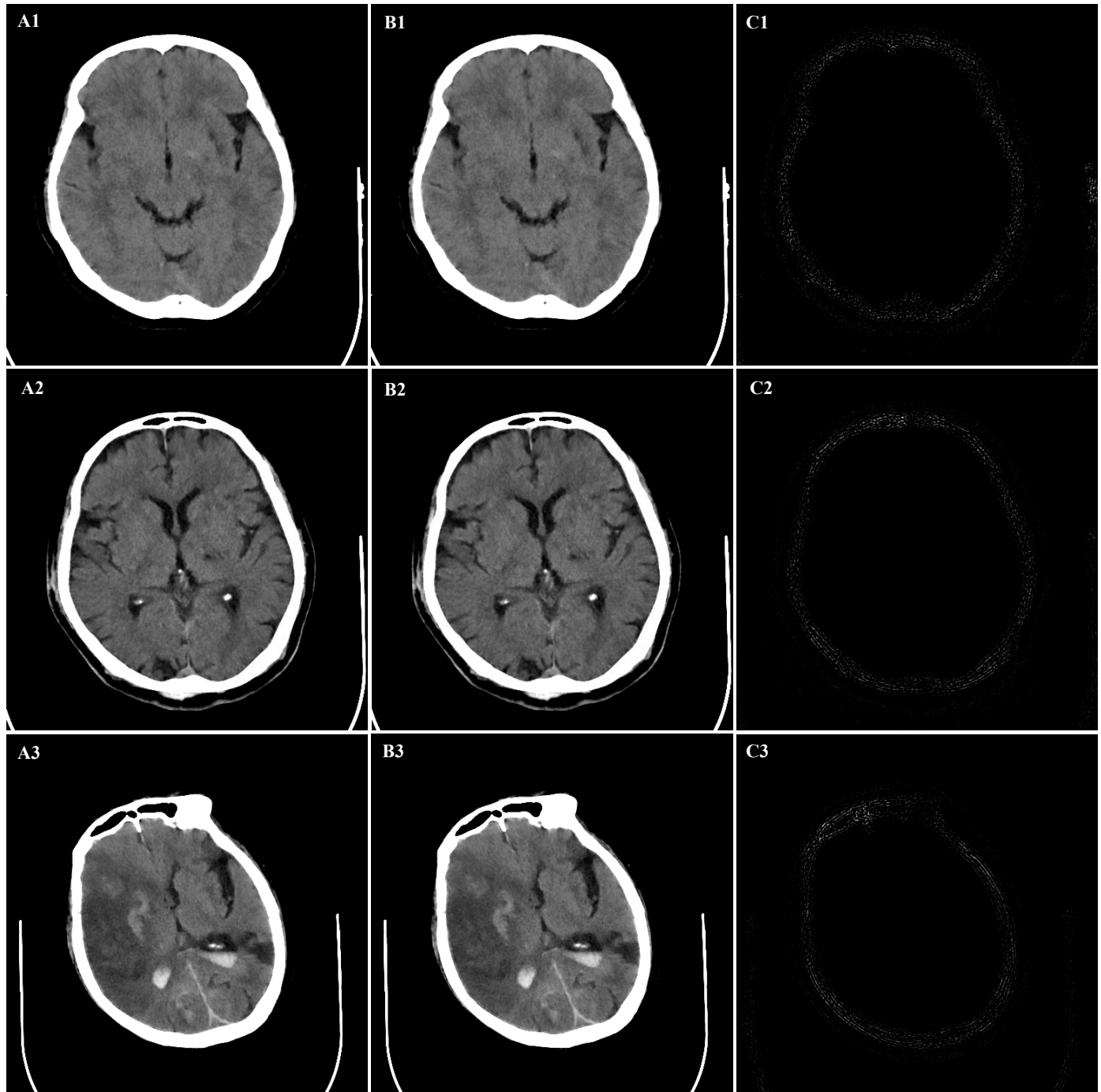


Fig.5 Sensitivity analysis of different dictionary options. A1, A2 and A3 correspond to the DL processed images using the dictionary trained from the LDCT images themselves; B1, B2 and B3 correspond to the DL processed images using the global dictionary; C1, C2 and C3 display the difference images between A1, A2, and A3 and B1, B2 and B3.

4. Discussion

Visual results in Fig.3-Fig.4 show that the proposed DL processing can provide effective suppression of both noise and

artifacts for the LDCT images. To be specific, the processed LDCT50% images have similar image quality to the reference SDCT images, and the processed LDCT25% images suffer some detail ambiguity and artifact residuals. Table 3 shows the DL processing produces images with even higher SNR and CNR than the reference images. In the qualitative tests using five subjective image scores from independent readers, notable improvement were seen from above comparison with original LDCT images. Especially the processed LDCT50% images are found to have no significant difference with reference to the original SDCT images ($P=0.18$) for all the subjective scores. Noise and artifacts were effectively suppressed without obvious loss of image details in the LDCT50% images. As to the processed LDCT25% images, the noise suppression, artifact suppression and overall image quality are also observed to have no significant difference from the reference SDCT image, but significant differences are found for contrast preservation and tissue discrimination.

With no access requirement of well-formatted raw data, the proposed processing can be easily applied to almost all the existing CT systems. The proposed approach can be efficiently implemented by using a pre-calculated global dictionary and multi-core parallelized computation. But we also observe some tiny structure blurring in the proposed DL image. Also, the whole computation cost of the DL processing still needs further acceleration to fulfill practical clinical requirements. Currently, some parameters (e.g. the sparsity level) still need to be empirically set. Future work will thus be devoted to further improve the image quality by incorporating some artifact-suppressing constraints from available SDCT image information [40], accelerating the computation in DL processing, and developing more robust parameter estimation. We will also explore the potential effects of segmentation/registration that might result from the proposed LDCT processing [41-42].

5. Conclusion

The proposed algorithm is robust in suppressing image noise and artifacts without obvious losing of image details and pathological changes. Our study supports the utilization of the proposed DL processing as a valuable tool for dose reduction in nonenhanced head CT.

Acknowledgments

This research was supported by National Basic Research Program of China (2010CB732503), National Natural Science Foundation (81370040, 31100713), and the Natural Science Foundation of Jiangsu Province (BK2011593), This work was also supported by the Key Laboratory of Computer Network and Information Integration (Southeast University), Ministry of Education.

References

- [1] Patient safety: Radiation dose in X-ray and CT Exams. http://www.radiologyinfo.org/en/safety/index.cfm?pg=sfty_xray. Accessed August 22, 2012
- [2] Kak AC and Slaney M. *Principles of Computerized Tomographic Imaging*. Philadelphia, PA: SIAM, 2001
- [3] Brenner DJ and Hall EJ. Computed tomography-an increasing source of radiation exposure. *New England Journal of Medicine* 2007;357: 2277-2284
- [4] Smith-Bindman R, Lipson J, Marcus R, et al. Radiation dose associated with common computed tomography examinations and the associated lifetime attributable risk of cancer. *Arch Intern Med*. 2009;169: 2078-2086
- [5] Kalra MK and Michael MM, et al. Strategies for CT Radiation Dose Optimization. *Radiology* 2004;230: 619-628
- [6] Yazdi M, Beaulieu L. Artifacts in Spiral X-ray CT Scanners: Problems and Solutions. *International Journal of Biological and Medical Sciences* 2008;4: 135-139
- [7] Xu J, Mahesh M, Tsui BM. Is iterative reconstruction ready for MDCT? *J Am Coll Radiol* 2009; 6:274-276
- [8] Thibault JB, Sauer K, Bouman C, et al. A three-dimensional statistical approach to improved image quality for multislice helical CT. *Med. Phys.* 2007; 34:4526-4544
- [9] Sidky E and Pan X. Image reconstruction in circular cone-beam computed tomography by constrained, total-variation minimization. *Phys. Med. Biol.* 2008; 53: 4777-4807
- [10] Chen Y, Feng Q, Luo L, et al. Nonlocal Prior Bayesian Tomographic Reconstruction. *Journal of Mathematical Imaging and Vision* 2008;30:133-146
- [11] Chen Y, Luo L, Chen W, et al. Bayesian statistical reconstruction for low-dose X-ray computed tomography using an adaptive-weighting nonlocal prior. *Computerized Medical Imaging and Graph* 2009;33: 495-500
- [12] Lubner M, Pickhardt P, Tang J, et al. Reduced image noise at low-dose multidetector CT of the abdomen with prior image constrained compressed sensing algorithm. *Radiology*, 2011;260: 248-256
- [13] Silva A, Lawder H, Hara A, et al. Innovations in CT dose reduction strategy: application of the adaptive statistical iterative reconstruction algorithm. *Am J Roentgenol* 2010;194: 191-199
- [14] Rapalino O, Kamalian S, et al. Cranial CT with adaptive statistical iterative reconstruction: improved image quality with concomitant radiation dose reduction. *Am J Neuroradiol* 2012; 33:609-615

- [15] Kilic K, Erbas G, Guryildirim M, et al. Lowering the dose in head CT using adaptive statistical iterative reconstruction. *Am J Neuroradiol* 2011;32:1578-1582
- [16] Korn A, Fenchel M, Bender B, et al. Iterative reconstruction in head CT: image quality of routine and low-dose protocols in comparison with standard filtered back-projection. *Am J Neuroradiol* 2012;33:218-224.
- [17] Wu TH, Hung SC, Sun JY, et al. How far can the radiation dose be lowered in head CT with iterative reconstruction? Analysis of imaging quality and diagnostic accuracy. *Europe Radiology*, 2013;DOI 10.1007/s00330-013-2846-6
- [18] Leipsic J, Nguyen G, Brown J, et al. A prospective evaluation of dose reduction and image quality in chest CT using adaptive statistical iterative reconstruction. *AJR Am J Roentgenol* 2010;195:1095-99
- [19] Singh S, Kalra M, Hsieh J, et al. Abdominal CT, comparison of adaptive statistical iterative and filtered back projection reconstruction techniques. *Radiology* 2010;257:373-383
- [20] Lewic MS, Olshausen BA, Field DJ. Emergence of simple-cell receptive field properties by learning a sparse code for natural images. *Nature*, 1996; 381:607-609
- [21] Lewicki MS, Sejnowski TJ. Learning overcomplete representations. *Neural Comput* 2000; 12:337-365
- [22] Delgado KK, Murray JF, et al. Dictionary learning algorithms for sparse representation. *Neural Comput* 2003;15:349-396
- [23] Donoho DL and Elad D. Maximal sparsity representation via l1 minimization. *Proc. Nat. Aca. Sci* 2003; 100:2197-2202
- [24] Elad M and Aharon M. Image denoising via sparse and redundant representations over learned dictionaries. *IEEE Transactions on Image Processing* 2006; 15: 3736-3745
- [25] Mairal J, Elad M, and Sapiro G. Sparse representation for color image restoration. *IEEE Transactions on Image Processing* 2007;17: 53-69
- [26] Mairal J, Sapiro G, and Elad M. Learning multiscale sparse representations for image and video restoration. *SIAM Multiscale Modeling and Simulation* 2008;7: 214-241
- [27] Wright J, Yang AY, Ganesh A, et al. Robust face recognition via sparse representation. *IEEE Transactions on Pattern Analysis and Machine Intelligence* 2008;31: 210-227
- [28] Ravishankar S and Bresler Y. MR Image Reconstruction from Highly Under sampled k-space Data by Dictionary Learning. *IEEE Transaction on Medical Imaging* 2011; 30: 1028-1041.
- [29] Ma L, Moisan L, Yu J, et al. A Dictionary learning approach for Poisson image deblurring. *IEEE Transactions on Medical Imaging* 2013; 32: 1277-1289.
- [30] Yu H and Wang G. Compressed sensing based interior tomography. *Phys. Med. Biol.*2009; 54:2791-805.
- [31] Xu Q, Yu H, Mou X, et al. Low-Dose X-ray CT Reconstruction via Dictionary Learning. *IEEE Transaction on Medical Imaging*, 2012;31: 1682-1697
- [32] Li S, Fang L, and Yin H. An efficient dictionary learning algorithm and its application to 3-D medical image denoising. *IEEE Transaction on Biomedical Engineering* 2012; 59: 417-427.
- [33] Lu Y, Zhao J, Wang G. Few-view image reconstruction with dual dictionaries. *Phys. Med. Biol.*2012; 57:173-189.
- [34] Zhao B, Ding H, Lu Y, Wang G, et al, Dual-dictionary learning-based iterative image reconstruction for spectral computed tomography application. *Phys. Med. Biol.* 2012; 57:8217-8229.
- [35] Chen Y, Yin X, Shi L, et al. Improving abdomen tumor low-dose CT images using a fast dictionary learning based processing. *Phys. Med. Biol.* 2013;58:5803-5820.
- [36] Heaney D E, Norvill C A J. A comparison of reduction in CT dose through the use of gantry angulations or bismuth shields. *Australasian Physics & Engineering Sciences in Medicine*, 2006, 29(2): 172-178.
- [37] Jessen KA, Panzer W, Shrimpton PC, et al. EUR 16262: European Guidelines on Quality Criteria for Computed Tomography. Paper presented at: Office for Official Publications of the European Communities; Luxembourg, 2000
- [38] Shrimpton PC, Hillier MC, Lewis MA, et al. National survey of doses from CT in the UK: 2003. *Br J Radiol.* Dec 2006; 79(948):968-980
- [39] Hakansson M, Svensson S, Zachrisson S, et al. ViewDEX 2.0: a Java-based DICOM-compatible software for observer performance studies. *Proc SPIE* 2009; 7263: 72631G1-72631G10
- [40] Chen Y, Yang Z, Hu Y, et al. Thoracic low-dose CT image processing using an artifact-suppressed large-scale nonlocal means. *Phys. Med. Biol.* 2012;57:2667-2688
- [41] Feng Q, Foskey M, Chen W, et al. Segmenting CT prostate images using population and patient-specific statistics for radiotherapy. *Med. Phys.* 2010;37: 4121-4132
- [42] Yang J, Wang YT, Chen WF, et al. Multiresolution elastic registration of X-Ray angiography images using thin-plate spline. *IEEE Transactions on Nuclear Science*, 2007; 54:152-166.